Nano Research

Open Access

Research Article

Multienzyme-mimetic MnO_2 aerogels with NIR-enhanced ROS regulation for treating MRSA-infected diabetic wounds

Minghui Wang[1], Jinkang Zheng[1], Dajun Rao[1], Yaxi Chen[1], Sihang Sun[2], Wenxin Que[2], Hongyu Gong[1], Wenchao Wu[1], Jing Tang[2] ✉, Qinglai Yang[1,2] ✉, and Xiaofeng Tan[1,2] ✉

[1] *Department of Hepatopancreatobiliary Surgery, The First Affiliated Hospital & Center for Molecular Imaging Probe, Cancer Research Institute & MOE Key Lab of Rare Pediatric Disease & NHC Key Laboratory of Neurodegenerative Diseases, Hengyang Medical School, University of South China, Hengyang 421001, China*

[2] *Department of Anesthesiology, Hunan Provincial Maternal and Child Health Care Hospital & NHC Key Laboratory of Birth Defect Research and Prevention, Hengyang Medical School, University of South China, Changsha 421001, China*

Cite this article: *Nano Research*, **2026**, *19*, 94908653. https://doi.org/10.26599/NR.2026.94908653

ABSTRACT: Diabetes mellitus represents a global health crisis, with an ever-growing population of patients suffering from chronic, non-healing diabetic wounds. These wounds are marked by a hostile microenvironment characterized by hyperglycemia, oxidative stress, inflammation, hypoxia, and bacterial colonization, all of which severely impair tissue regeneration and angiogenesis. Amid these interrelated pathological factors, regulating reactive oxygen species (ROS) dynamics has emerged as a key therapeutic strategy. Appropriate spatiotemporal control of ROS is critical: insufficient ROS in the early stages of infection compromises antimicrobial defense, whereas excessive ROS accumulation during the inflammatory phase induces oxidative damage and sustains chronic inflammation. To simultaneously modulate ROS and address the multifactorial diabetic wound microenvironment, herein we present a multifunctional manganese dioxide (MnO_2) aerogel synthesized via a freeze-thaw method in a water/N,N-dimethylformamide (DMF) mixture, forming a three-dimensional (3D) interconnected network with hierarchical porosity and nanoflower-like morphology. The MnO_2 aerogel mimics five key enzyme-like activities—oxidase, glucose oxidase (GOx), glutathione peroxidase (GPX), catalase (CAT), and superoxide dismutase (SOD)—thereby enabling antibacterial, antioxidant, glucose-regulating, and tissue-regenerative functions. Additionally, near-infrared (NIR) photothermal activation further augments its antimicrobial efficacy by disrupting bacterial biofilms and promoting ROS generation. Taken together, *in vitro* and *in vivo* experiments reveal that MnO_2 aerogels significantly attenuate inflammation, re-establish glucose and redox homeostasis, and accelerate wound closure by enhancing angiogenesis and tissue regeneration. This work highlights metallic oxide aerogel as a promising platform for advanced diabetic wound therapy, providing an integrated strategy to address the complex challenges of wound management.

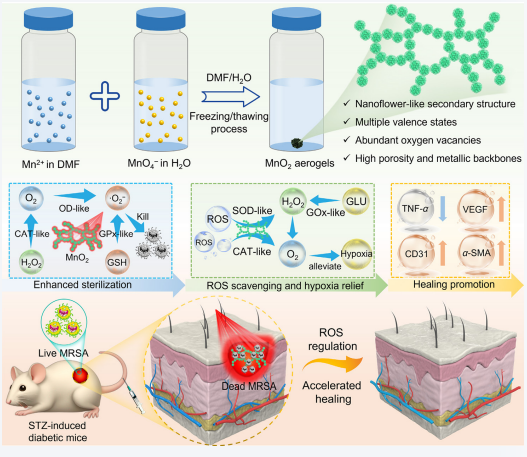

KEYWORDS: diabetes, oxidative stress, near-infrared, MnO_2 aerogels, metallic oxide aerogel, photothermal therapy

1 Introduction

Diabetes mellitus, a significant global health concern, is expected to affect over 1.3 billion individuals by 2050 [1, 2]. As the worldwide impact of diabetes grows, the complexity of managing its complications, particularly chronic diabetic wounds, becomes increasingly challenging [3, 4]. These wounds, which are notoriously difficult to heal, prolong patient suffering and substantially impair quality of life. At the core of this challenge lies the disruption of normal wound healing processes, driven by the unique and hostile microenvironment associated with diabetic wounds [5, 6]. Chronic diabetic wounds are characterized by a persistent cycle of hyperglycemia, prolonged inflammation,

Received: January 8, 2026; **Revised:** March 15, 2026
Accepted: March 18, 2026

✉Address correspondence to Jing Tang, tangjing-read@outlook.com; Qinglai Yang, qingyu513@usc.edu.cn; Xiaofeng Tan, tanxiaofeng@usc.edu.cn

oxidative stress, hypoxia, and microbial colonization [7–10]. Together, these factors create a pathological environment that severely impairs angiogenesis and tissue regeneration [11]. Reactive oxygen species (ROS) are crucial in this impaired microenvironment. During the initial stages of infection, ROS are key mediators of the body's antimicrobial defense, capable of disrupting bacterial structures and killing pathogens [12, 13]. However, as inflammation persists, excessive ROS accumulation exacerbates tissue damage by attacking cellular components and hindering the healing process [14, 15]. This imbalance suppresses regenerative pathways, particularly in immune cells such as macrophages. As a result, macrophages fail to convert from a pro-inflammatory M1 phenotype to a reparative M2 phenotype and exhibit reduced secretion of the anti-inflammatory cytokine interleukin-10 (IL-10) and regeneration-promoting factors like tumor necrosis factor-α (TNF-α), epidermal growth factor (EGF) and vascular endothelial growth factor (VEGF) [16–18]. Despite extensive research into diabetic wound healing, conventional therapeutic strategies—including hyperbaric oxygen therapy, topical treatments, glycemic control, and antibiotics—have met with limited success, often yielding suboptimal outcomes and undesirable side effects [19–21]. Thus, there is an urgent need for more effective, multifunctional approaches that can not only combat infections but also alleviate inflammation and enhance tissue regeneration. Among the emerging options, strategies that precisely modulate ROS levels offer a particularly promising avenue for improving the diabetic wound-healing microenvironment [22–24].

Despite the promise of ROS modulation in diabetic wound healing, most current treatments remain limited by issues such as instability, uncontrolled release, and poor tissue penetration [25]. Artificial enzyme mimics, or nanozymes, have emerged as promising candidates for overcoming these challenges [26, 27]. Nanozymes, including those mimicking natural enzymes like superoxide dismutase (SOD), catalase (CAT), and glucose oxidase (GOx), offer advantages in terms of stability, cost-effectiveness, and enhanced enzymatic activity [28–30]. Despite their potential, existing nanozymes still suffer from suboptimal biocompatibility, predominantly unidirectional ROS regulation, and an inability to address the multifaceted pathology of diabetic wounds. To address these shortcomings, metal oxide aerogels, particularly those based on manganese dioxide (MnO_2), have attracted increasing attention because of their unique structural properties, including high porosity, conductive metallic backbones, and self-supporting features. These characteristics allow for efficient access to reactive centers and optimized diffusion of reactants, enabling precise control over ROS levels in wound sites [31, 32]. Moreover, the multiple valence states and abundant defect sites (e.g., oxygen vacancies) in MnO_2 confer multienzyme-like activity and photothermal responsiveness, supporting antibacterial, anti-inflammatory, and regenerative effects [33]. However, a comprehensive, multifunctional platform that fully integrates these structural and catalytic advantages for advanced diabetic wound therapy remains largely underexplored.

Herein, we designed a multifunctional MnO_2 aerogel using a freezing/thawing technique in a water/N,N-dimethylformamide (DMF) mixture. The resulting self-assembled MnO_2 aerogels exhibit a three-dimensional (3D) interconnected network with multilevel pores and flower-like morphologies composed of intersecting ultrathin nanosheets. Leveraging this unique architecture, the MnO_2 aerogels mimic five enzyme functions—oxidase (OD), GOx, glutathione peroxidase (GPX), CAT, and SOD—thereby providing coordinated antibacterial, glucose-regulating, antioxidant, and tissue-regenerative effects in diabetic wound therapy. In addition, their strong near-infrared (NIR) photothermal responsiveness serves as an external trigger that further amplifies these therapeutic functions. The OD-like activity facilitates the generation of superoxide anions ($\cdot O_2^-$) from dissolved O_2 for effective sterilization, offering strong bactericidal effects without the tissue-damaging risks associated with peroxidase (POD)-like nanozymes that require exogenous hydrogen peroxide (H_2O_2). Under NIR irradiation, localized photothermal heating disrupts bacterial membranes and enhances OD-like activity, synergistically breaking down biofilms and inhibiting microbial growth. Meanwhile, the GOx-like and GPX-like activities of the MnO_2 aerogels consume excess glucose and deplete glutathione (GSH), thereby amplifying ROS generation within the wound microenvironment. Notably, during the subsequent inflammatory phase, the CAT-like and SOD-like properties of the MnO_2 aerogels scavenge excess ROS and alleviate hypoxia, restoring cellular redox balance disrupted by hyperglycemia-induced dysfunction. *In vivo* experiments further demonstrated that MnO_2 aerogel treatment, particularly when combined with NIR irradiation, markedly downregulated TNF-α and reduced inflammatory cell infiltration, while upregulating VEGF, alpha-smooth muscle actin (α-SMA), and cluster of differentiation 31 (CD31), indicative of robust neovascularization. These anti-inflammatory and pro-angiogenic effects, arising in part from the CAT-like decomposition of H_2O_2 into O_2 that relieves hypoxia in the infected microenvironment, ultimately accelerate diabetic wound healing by eliminating pathogens, reduction of local wound glucose levels, dynamically regulating ROS, and promoting angiogenesis (Scheme 1).

2 Results and discussion

2.1 The fabrication and characterization of the MnO_2 aerogels

MnO_2 aerogels were produced by reducing MnO_4^- with Mn^{2+} in a water/DMF mixture (Fig. 1(a)). Briefly, the resulting black solution was rapidly frozen in liquid nitrogen to form a dark-gray solid, and then lyophilized in a freeze-dryer to yield a monolithic MnO_2 aerogel while minimizing the structural changes. Scanning electron microscopy (SEM) image of MnO_2 aerogels revealed a 3D interconnected network with multilevel pores and flower-like morphologies (Fig. 1(b)). Transmission electron microscopy (TEM) further confirmed the flower-like nanoparticle structure, which have a diameter of about 226 nm and are made up of intersecting ultrathin nanosheets (Figs. 1(c) and 1(d)). High-resolution TEM (HRTEM) showed curled and folded nanosheets with a lattice spacing of 0.28 nm, corresponding to the (002) plane of face-centered cubic MnO_2 (Fig. 1(e)). Selected area electron diffraction (SAED) displayed four distinct diffraction rings, confirming the polycrystalline nature of the MnO_2 aerogels (Fig. S1 in the Electronic Supplementary Material (ESM)). High-angle annular dark-field scanning TEM (HAADF-STEM) and elemental mapping demonstrated uniform distribution of Mn and O across the nanoflower structures, indicating homogeneous growth and dispersion of MnO_2 within the aerogel framework (Figs. 1(f)–1(i)). X-ray photoelectron spectroscopy (XPS) further verified the

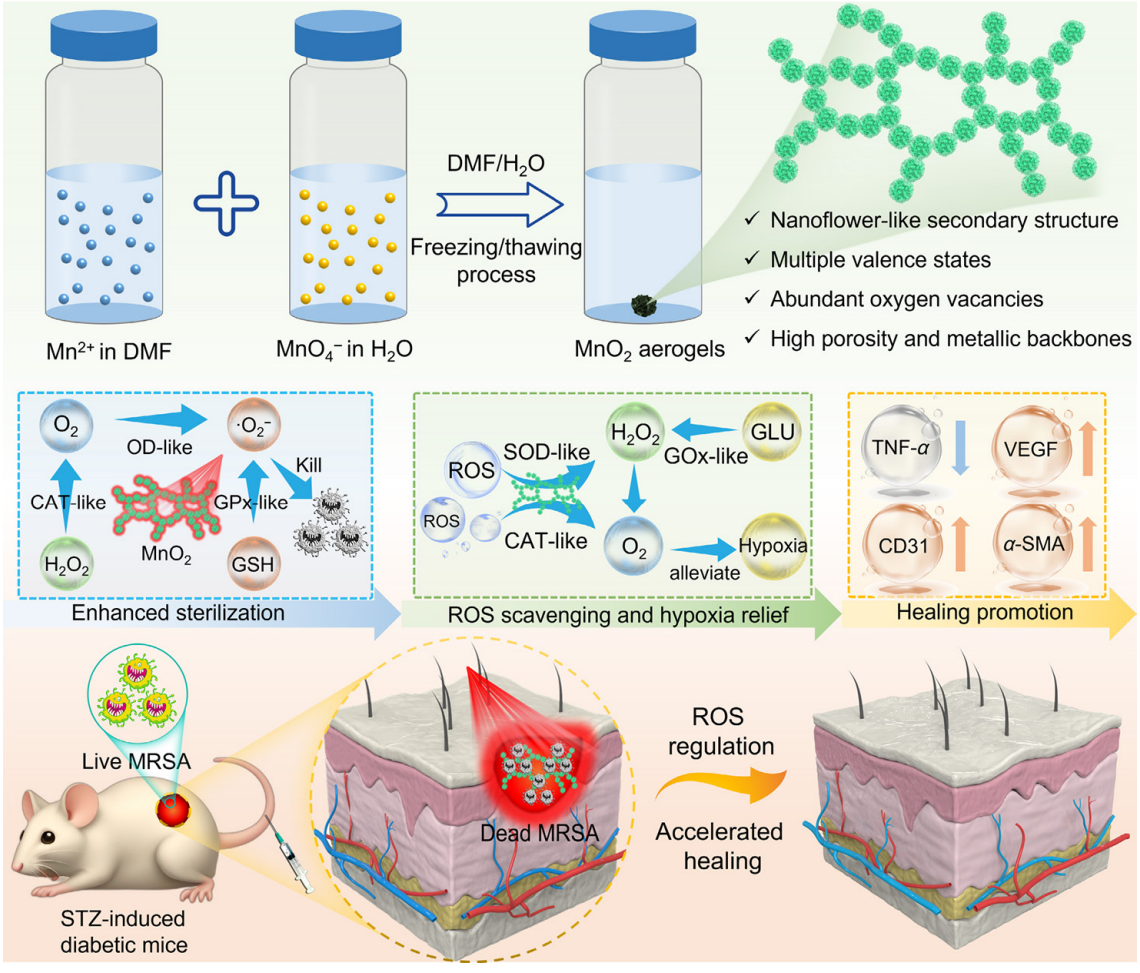

Scheme 1 Schematic illustration of the process for constructing MnO_2 aerogels and their applications in antibacterial therapy and promotion of healing in diabetic wounds.

presence of Mn and O, with the Mn 2p spectrum splitting into Mn $2p_{3/2}$ and Mn $2p_{1/2}$ peaks (energy separation: 11.8 eV), indicating Mn^{3+} (640.1 eV) and Mn^{4+} (641.9 eV) oxidation states, which can be attributed to oxygen vacancies-induced conversion from stable d^3 (Mn^{4+}) to unstable d^4 (Mn^{3+}) (Figs. 1(j) and 1(k)). The O 1s XPS spectrum revealed peaks at 529.7 eV (lattice oxygen, Mn–O–Mn), 531.7 eV (oxygen vacancies), and 533.4 eV (adsorbed oxygen), respectively (Fig. 1(l)). N_2 adsorption-desorption isotherms analysis showed that the specific surface area of the MnO_2 aerogels was 182.16 m^2/g, indicating high surface exposure. Pore size distribution analysis confirmed its hierarchically porous structure (Fig. S2 in the ESM). X-ray diffraction (XRD) showed peaks at 12.04°, 24.74°, 36.84°, and 65.72°, matching the (001), (002), ($\bar{1}$11), and (020) planes of δ-MnO_2 (PDF#80-1098) (Fig. 1(m)). Electron spin resonance (ESR) analysis detected a signal at g = 2.003, confirming the presence of oxygen vacancies (Fig. S3 in the ESM). Oxygen vacancies, defects formed by the loss of oxygen ions from the MnO_2 lattice, are critical to the catalytic performance of MnO_2 aerogels. Specifically, oxygen vacancies can alter the local electronic structure of MnO_2 by increasing electron density asymmetry and promoting the coexistence of mixed Mn valence states (e.g., Mn^{3+}/Mn^{4+}). These defect sites can serve as catalytically active centers with enhanced electron-transfer capability, thereby facilitating the adsorption and activation of reactants such as dissolved O_2, H_2O_2, and reactive oxygen intermediates. In this context, the OD-like and POD-like activities are associated with more efficient electron transfer from the catalytic centers to adsorbed oxygen-containing species, leading to ROS generation, whereas the CAT-, SOD-, and GPX-like activities are related to defect-assisted redox cycling of manganese centers that promotes ROS conversion and disproportionation. The hierarchical porous aerogel framework exposes abundant defect-rich active sites and improves accessibility of reactants to the catalytic surface, while the interconnected network facilitates mass transport. In addition, under NIR irradiation, the photothermal effect further accelerates interfacial reaction kinetics and charge-transfer processes, which is favorable for enhancing the overall enzyme-like catalytic performance.

2.2 Assessment of photothermal and multienzyme-like activity of MnO_2 aerogels

MnO_2 aerogels exhibited strong UV–vis–NIR absorption across a broad spectrum, with intensity increasing with concentration (Fig. 2(a)). When exposed to an 808 nm laser at 1.0 W/cm^2 for 10 min, the temperature of MnO_2 aerogel solutions (200 μg/mL) rose by approximately 25 °C compared to a 3 °C rise in phosphate-buffered saline (PBS) (Fig. 2(b)). The temperature elevation showed a positive correlation with both MnO_2 aerogel concentration and laser power density (Figs. S4 and S5 in the ESM). Good photothermal stability was confirmed by consistent temperature profiles over four irradiation-cooling cycles, matching the initial

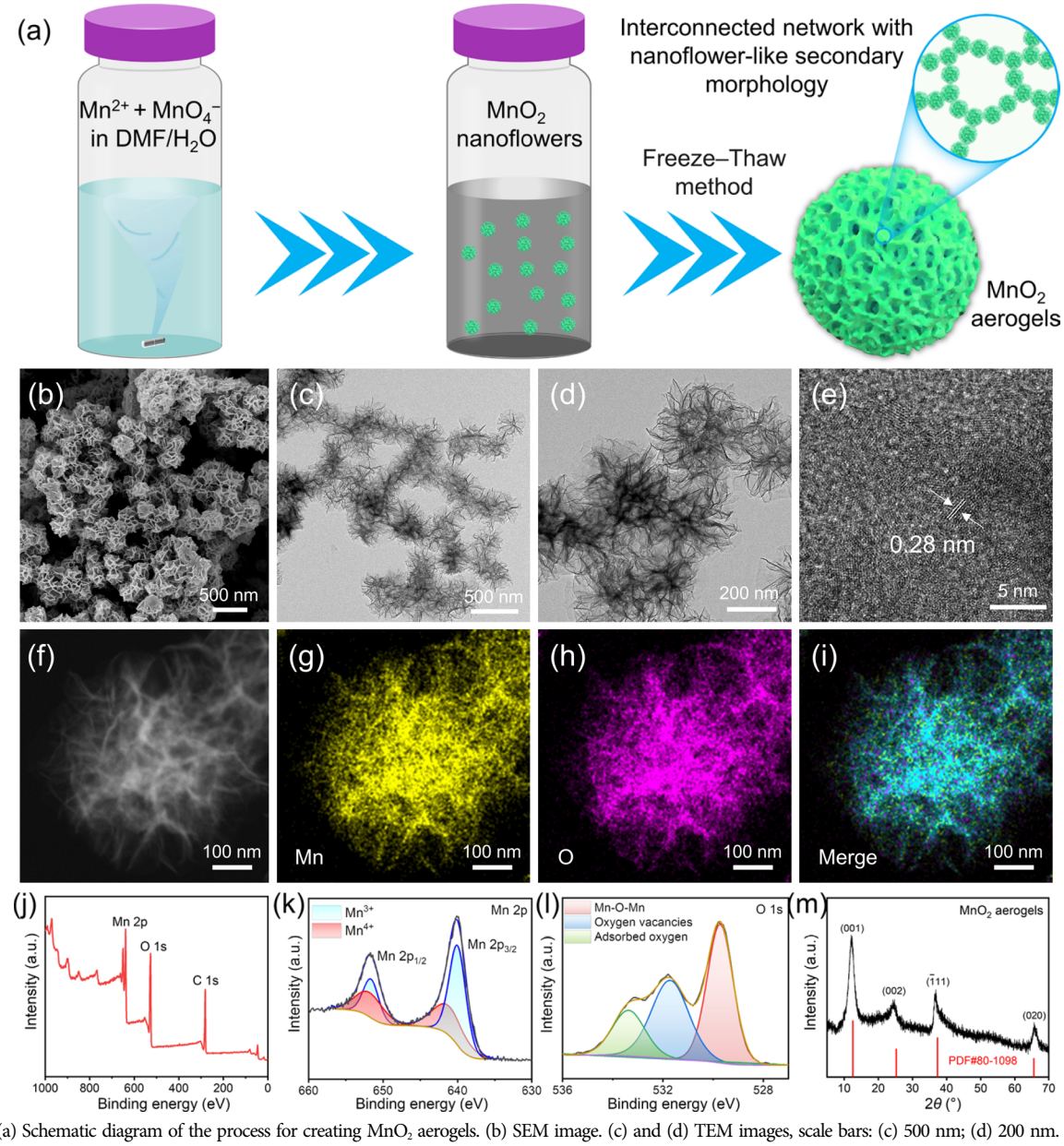

Figure 1 (a) Schematic diagram of the process for creating MnO_2 aerogels. (b) SEM image. (c) and (d) TEM images, scale bars: (c) 500 nm; (d) 200 nm. (e) HRTEM image. (f) HAADF-STEM image. Corresponding element mapping images of (g) Mn, (h) O and (i) the merged map. (j) Broad XPS spectrum. Peak-fitting XPS spectra of (k) Mn 2p and (l) O 1s. (m) XRD patterns of MnO_2 aerogels.

cycle (Fig. S6 in the ESM). The photothermal conversion efficiency (PCE), η, was determined as 36.3% using heating-cooling curves and equations in the ESM, demonstrating that MnO_2 aerogels act as efficient photothermal agents for photothermal therapy (PTT) (Fig. 2(c)). The oxidase-like (OD-like) activity of MnO_2 aerogels was evaluated through the 3,3',5,5'-tetramethylbenzidine (TMB) colorimetric assay, showing a characteristic oxTMB peak at 652 nm in the presence of dissolved O_2 (Fig. 2(d)). This activity was optimal across a pH range of 2–10 (Fig. S7(a) in the ESM), enhanced in O_2-saturated conditions, and inhibited under N_2-saturated conditions (Fig. 2(e)). The OD-like activity was concentration-dependent and stable between 10–70 °C owing to the robust structure of the MnO_2 aerogels (Figs. S7(b) and S7(c) in the ESM). Steady-state kinetics experiments determined that the V_{max} of the MnO_2 aerogels for TMB is 3.00×10^{-8} M/s, with a K_m value of 0.0215 mM (Fig. S8 in the ESM). Compared with previously reported MnO_2-based nanozymes (Table S1 in the ESM), the MnO_2 aerogels exhibits superior substrate affinity. ROS production, specifically superoxide ($\cdot O_2^-$), was confirmed using dihydroethidium (DHE) probe, which showed an increased absorption peak at 480 nm (Fig. S9(a) in the ESM). Using electron spin resonance (ESR) spectroscopy with 5,5-dimethyl-1-pyrroline N-oxide (DMPO) as the spin-trapping agent, a characteristic six-line signal of $\cdot O_2^-$ (with the intensity of 1:1:1:1:1:1) was observed, thus further confirming the generation of $\cdot O_2^-$ (Fig. S9(b) in the ESM). The GOx-like activity of MnO_2 aerogels was evaluated by detecting the pH changes of the incubation solution resulting from gluconic acid formation. Upon incubation of glucose with increasing concentrations of MnO_2 aerogels, the solution pH gradually decreased, indicating efficient GO_x-like catalytic oxidation of glucose by MnO_2 aerogels (Fig. 2(f)). Glucose consumption was directly measured using a glucose assay kit in the presence of the MnO_2 aerogels. The results indicated that

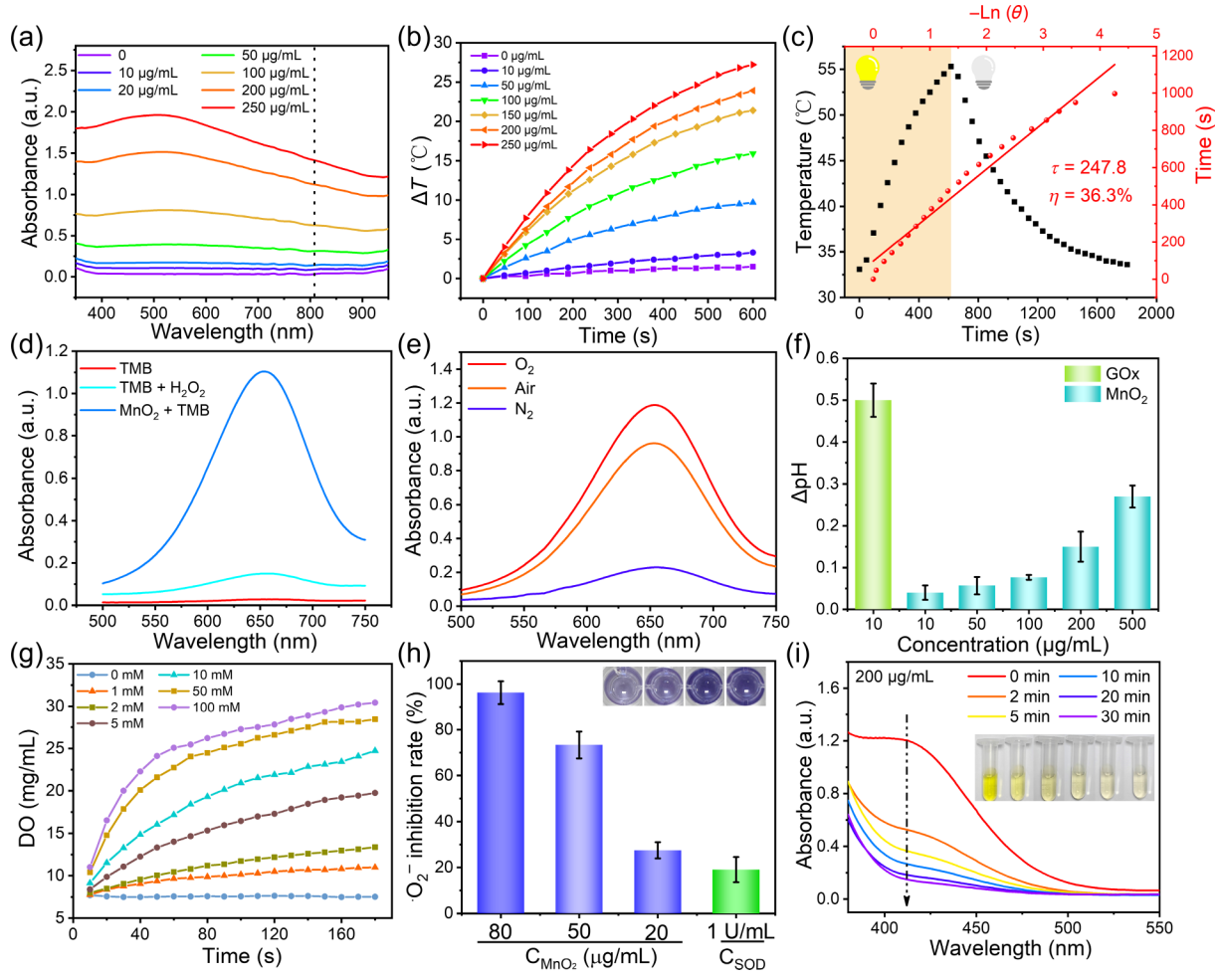

Figure 2 (a) UV–vis–NIR absorption spectra of different concentrations of MnO_2 aerogels. (b) Photothermal curves of MnO_2 aerogels with different concentrations irradiated with an 808 nm laser at 1 W/cm² for 10 min. (c) Calculation curves of photothermal conversion efficiency. (d) UV–vis spectral profiles of TMB solutions following different treatments. (e) Comparison of OD-like activities of MnO_2 aerogels under N_2- and O_2-saturated conditions. (f) Changes in pH after incubation with glucose at different concentrations of MnO_2 aerogels. (g) MnO_2 aerogels catalyze the production of O_2 at different concentrations of H_2O_2. (h) Ability of MnO_2 aerogels with different concentrations to remove $\cdot O_2^-$. (i) Time-dependent curves of GSH consumption by MnO_2 aerogels at 200 μg/mL.

MnO_2 aerogels could catalyze glucose consumption in a concentration-dependent manner, further demonstrating their GOx-like activity (Fig. S10 in the ESM). Catalase-like (CAT-like) activity was confirmed by increased dissolved O_2 levels in the presence of H_2O_2 (0–100 mM), measured with a dissolved oxygen meter (Fig. 2(g)), and corroborated by reduced H_2O_2 absorption at 240 nm (Fig. S11 in the ESM).

The dissolved oxygen levels in MnO_2 aerogels + H_2O_2 system increased significantly with the rising H_2O_2 concentration (0–100 mM), confirming that the MnO_2 aerogels effectively decompose H_2O_2 into O_2. SOD-like activity was assessed through the use of an SOD assay kit. The quantitative analysis exhibited 27.5% $\cdot O_2^-$ scavenging at 20 μg/mL, surpassing natural SOD (1 U/mL, 19%) (Fig. 2(h)). GSH depletion was assessed with a 5,5'-dithio-bis-(2-nitrobenzoic acid) (DTNB) probe, revealing a time- and concentration-dependent decrease in the 412 nm absorption peak, with complete GSH depletion at 500 μg/mL within 10 min (Fig. 2(i) and Fig. S12(a) in the ESM). Remarkably, MnO_2 aerogels at 500 μg/mL could completely deplete GSH within 10 min (Fig. S12(b) in the ESM). Consistently, the GSH depletion rate increased markedly with increasing MnO_2 aerogel concentration (Fig. S12(c) in the ESM). These multienzyme-like activities enhance the ROS-mediated antibacterial efficacy of MnO_2 aerogels in inflammatory microenvironments. To evaluate storage stability, MnO_2 aerogels were stored at 4 °C, and their OD-like activity was measured. The catalytic activity remained stable over one month, demonstrating good stability under low-temperature, dark, and dry conditions (Fig. S13 in the ESM). In addition, we investigated whether the photothermal property of MnO_2 aerogels could enhance their enzyme-like catalytic activity during antibacterial treatment. As shown in Fig. S14 in the ESM, upon NIR irradiation, the OD-like, CAT-like, and GPX-like activities of the MnO_2 aerogels increased by 6.2%, 23.5%, and 19.7%, respectively, compared with those without NIR irradiation. These results demonstrate that MnO_2 aerogels exhibit photothermally enhanced multi-enzyme-mimicking activities. Such enhancement is expected to further promote modulation of the bacterial microenvironment and thereby strengthen the antibacterial performance of the material.

2.3 Evaluation of antibacterial efficacy of MnO_2 aerogels *in vitro*

Based on the superior photothermal and multienzyme-like activities of MnO_2 aerogels, we hypothesized that they would exhibit potent antibacterial effects. Methicillin-resistant *Staphylococcus aureus*

(MRSA) and *Pseudomonas aeruginosa* (*P. aeruginosa*) were selected as examples of Gram-positive and Gram-negative bacteria, respectively. To assess *in vitro* antibacterial efficacy, bacteria were subjected to eight treatments: (I) Control, (II) Control + NIR, (III) Oxygenated PBS (OP, to avoid the influence of H_2O_2), (IV) OP + NIR, (V) MnO_2 aerogels, (VI) MnO_2 aerogels + NIR, (VII) MnO_2 aerogels + OP, and (VIII) MnO_2 aerogels + OP + NIR. Bacterial survival was quantified using the plate counting method. As shown in Figs. 3(a) and 3(b), the MnO_2 aerogels + OP + NIR group exhibited significantly fewer colonies than the MnO_2 aerogels + NIR group, indicating that oxygen supplementation markedly enhances antibacterial performance against both MRSA and *P. aeruginosa*. Quantitative analysis revealed a bacterial survival rate of 71.6% for the MnO_2 aerogels + OP group against MRSA, which was attributed to their OD-like activity and was lower than that of the control and OP groups with or without NIR (Fig. 3(c)). The MnO_2 aerogels + OP + NIR group achieved a survival rate of only 2.5%, significantly lower than the 30% observed in the MnO_2 aerogels + NIR group, demonstrating the synergistic effect of photothermal therapy (PTT) and nanozyme catalysis for broad-spectrum antibacterial activity (Fig. 3(d)).

The bactericidal effect was further validated using live/dead staining with the N01/PI kit, observed via confocal laser scanning microscopy (CLSM). Live bacteria exhibited green fluorescence (labeled with N01), while dead bacteria showed red fluorescence (labeled with PI). Consistent with plate counting results, groups without NIR irradiation displayed green fluorescence similar to the control group. In contrast, NIR-treated MnO_2 groups showed increased red fluorescence, with the MnO_2 aerogels + OP + NIR group exhibiting the highest proportion of dead bacteria, thereby confirming the enhanced antibacterial efficacy arising from synergistic PTT and nanozyme activity (Figs. 3(e)–3(h)).

SEM was used to qualitatively assess bacterial morphology after various treatments. In the control and OP groups, MRSA and *P. aeruginosa* maintained smooth membranes and intact spherical (MRSA) or rod-shaped (*P. aeruginosa*) structures (Figs. 4(a) and 4(b)). Treatment with MnO_2 aerogels alone caused slight surface depressions, while the MnO_2 aerogels + NIR group induced deep wrinkling, indicating partial photothermal damage to the bacterial cell envelope. Notably, the MnO_2 aerogels + OP + NIR group caused extensive wrinkles and dents, highlighting superior antibacterial capacity via oxygen-enhanced synergistic PTT/nanozyme therapy. ROS levels were assessed with the 2',7'-dichlorodihydrofluorescein diacetate (DCFH-DA) fluorescent probe. The results revealed higher ROS levels in the MnO_2 aerogels + OP + NIR group compared to other groups, further confirming the enhanced PTT/nanozyme combinatorial effect against planktonic bacteria (Figs. 4(c) and 4(d)).

Bacterial biofilms, known for their resistance to immune clearance and antibacterial treatments due to hypoxic zones, were investigated for their susceptibility to degradation by MnO_2 aerogels. Crystal violet staining showed that MnO_2 aerogels

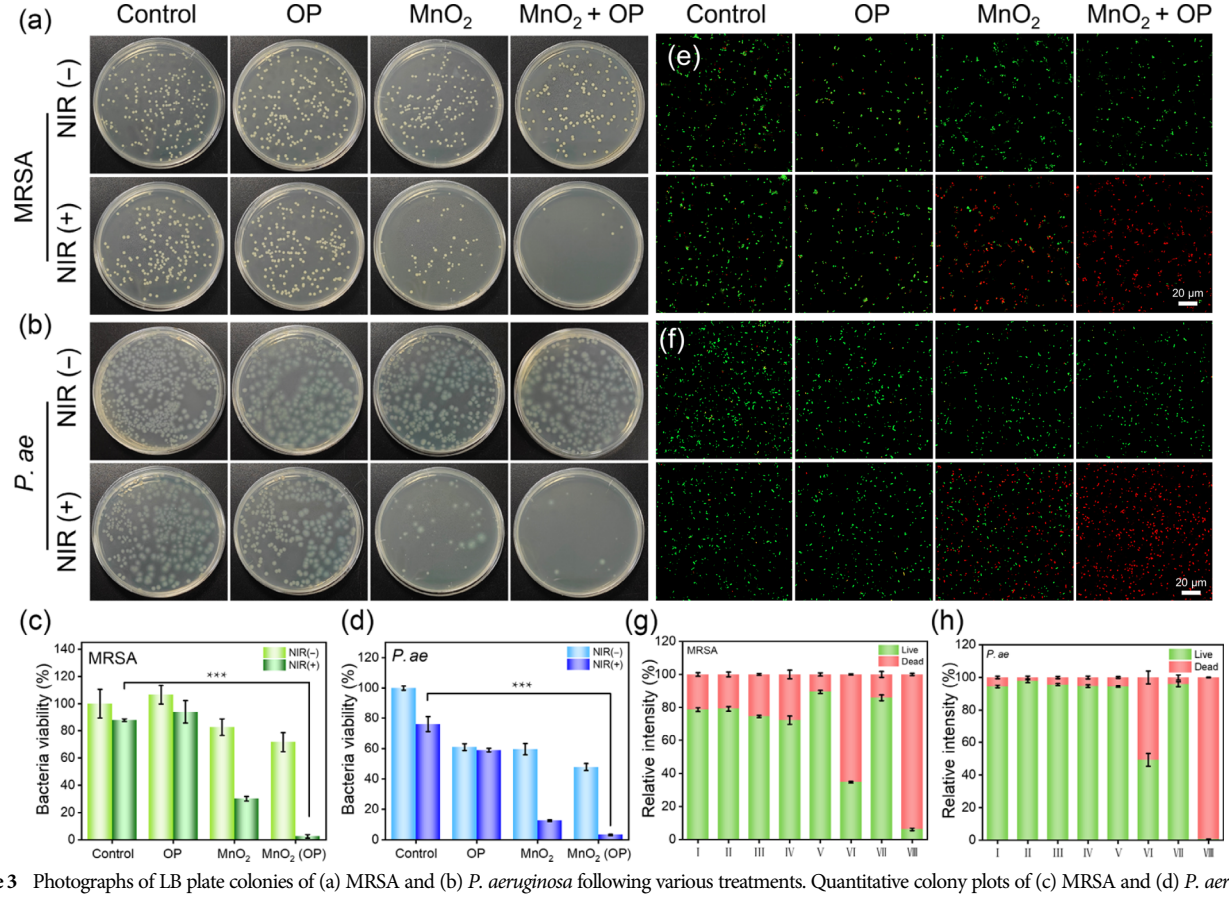

Figure 3 Photographs of LB plate colonies of (a) MRSA and (b) *P. aeruginosa* following various treatments. Quantitative colony plots of (c) MRSA and (d) *P. aeruginosa* after different treatments. Confocal microscopy images of (e) MRSA and (f) *P. aeruginosa* stained with live/dead bacteria after different treatments. Corresponding fluorescence quantification results of (g) MRSA and (h) *P. aeruginosa* (I: Control; II: Control + NIR; III: OP; IV: OP + NIR; V: MnO_2 aerogels; VI: MnO_2 aerogels + NIR; VII: MnO_2 aerogels + OP; VIII: MnO_2 aerogels + OP + NIR). The green fluorescent channel: λ_{ex} = 488 nm, λ_{em} = 525 nm. The red fluorescent channel: λ_{ex} = 540 nm, λ_{em} = 617 nm. $^*P < 0.05$, $^{**}P < 0.01$, $^{***}P < 0.001$.

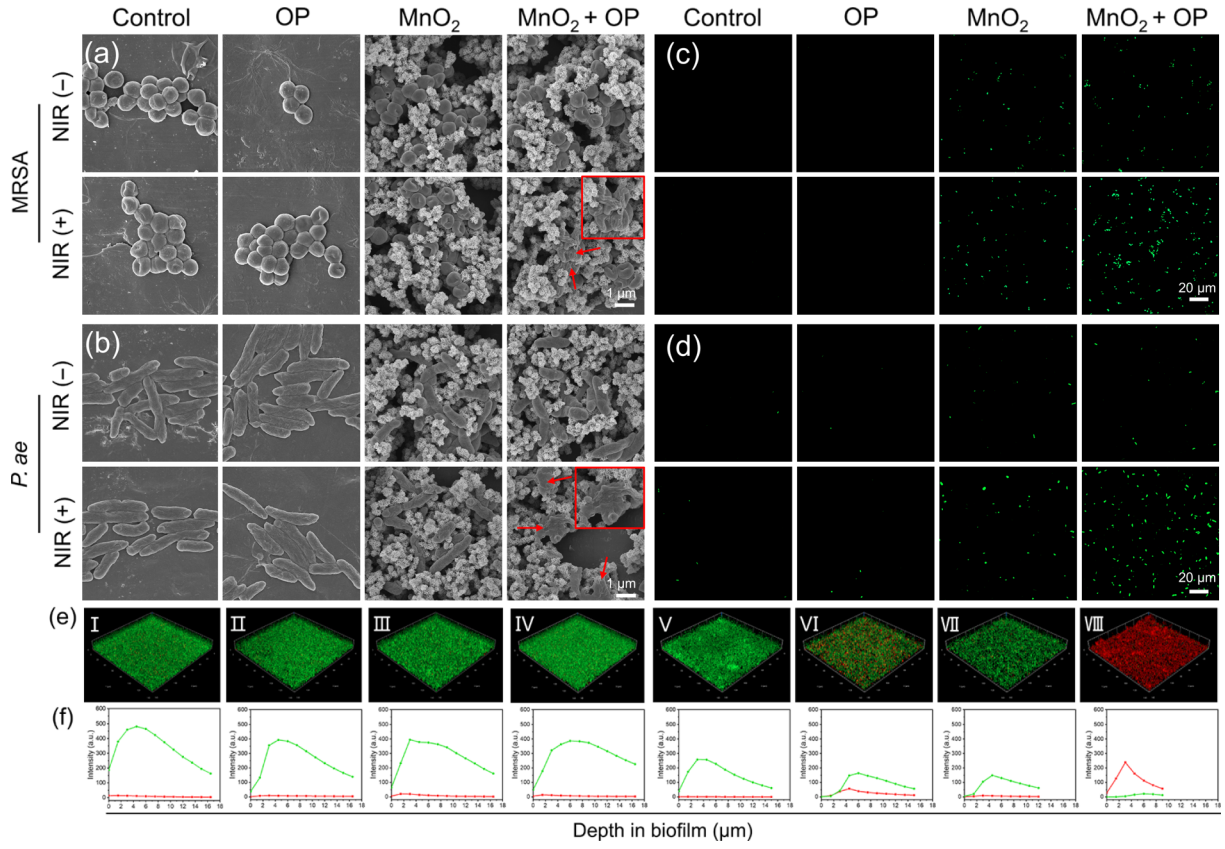

Figure 4 SEM images of (a) MRSA and (b) *P. aeruginosa* after different treatments. ROS fluorescence images of (c) MRSA and (d) *P. aeruginosa* after different treatments using DCFH-DA. Green fluorescence channel: λ_{ex} = 488 nm, λ_{em} = 525 nm. (e) 3D-CLSM images illustrating MRSA biofilms in different treatment groups (I: Control; II: Control + NIR; III: OP; IV: OP + NIR; V: MnO_2 aerogels; VI: MnO_2 aerogels + NIR; VII: MnO_2 aerogels + OP; VIII: MnO_2 aerogels + OP + NIR). (f) Quantified fluorescence intensity in each CLSM plane in (e) as a function of depth in the biofilm.

degraded 65%–70% of biofilms under NIR irradiation (Fig. S15 in the ESM). Three-dimensional CLSM with live/dead staining revealed that the *MRSA* biofilm in the MnO_2 aerogels + OP + NIR group was significantly thinner, with a predominance of red fluorescence signals, indicating substantial biofilm destruction compared to other groups (Figs. 4(e) and 4(f)). Collectively, these results underscore the potent biofilm-disrupting capability of MnO_2 aerogels, particularly under oxygen-enriched PTT conditions.

2.4 Antibacterial effect *in vivo* of MnO_2 aerogels on diabetic wounds

Diabetic chronic wounds are highly susceptible to bacterial infections and persistent inflammation due to a hyperglycemic microenvironment, which delays wound healing. Building on the potent *in vitro* antibacterial efficacy of MnO_2 aerogels, we evaluated their *in vivo* performance in a MRSA-infected diabetic wound model (Fig. 5(a)). All procedures were approved by the Institutional Animal Welfare and Ethics Review Committee of the University of South China and were carried out in accordance with its guidelines. Diabetes was induced in male Kunming mice (6–8 weeks old) via intraperitoneal injection of streptozotocin (STZ; 120 mg/kg in 0.1 M sodium citrate buffer, pH 4.5). Blood glucose levels ≥ 16.7 mmol/L, measured via tail vein 48 h post-injection, confirmed diabetes. On the backs of anesthetized mice, an 8 mm wound penetrating the full thickness was established and inoculated with 50 μL of MRSA suspension (1×10^8 CFU/mL). After 24 h, mice were randomly assigned to four groups (n = 3): (I) Control, (II) Control + NIR, (III) MnO_2 aerogels, and (IV) MnO_2 aerogels (200 μg/mL) + NIR. Wound temperatures were monitored using an infrared thermal camera, revealing a rapid increase to 45 °C within 5 min in the MnO_2 aerogels + NIR group, which demonstrated superior *in vivo* photothermal properties (Fig. S16 in the ESM). Wound size and body weight were recorded, and digital photographs were taken every two days for 12 days. The MnO_2 aerogels + NIR group achieved complete wound closure by day 12, while the control group exhibited significantly larger wounds, highlighting the synergistic effect of photothermal therapy (PTT)/nanozyme activity in promoting wound healing (Figs. 5(b) and 5(c)). Body weight remained stable across all groups, indicating good systemic biocompatibility of MnO_2 aerogels (Fig. 5(d)). On day 12, wound tissues were harvested for bacterial quantification via plate counting, showing the lowest colony counts in the MnO_2 aerogels + NIR group (Fig. 5(g)). Histopathological analysis using hematoxylin and eosin (H&E) staining revealed the fewest inflammatory cells and clear epidermal regeneration in the MnO_2 aerogels + NIR group (Fig. 5(e)). Masson's trichrome staining confirmed increased collagen fiber deposition in the MnO_2 aerogels + NIR group, supporting enhanced tissue regeneration (Fig. 5(f)).

Macrophage polarization is highly sensitive to the local redox microenvironment: persistent excessive ROS is generally associated with sustained pro-inflammatory M1-like activation, whereas restoration of redox homeostasis and attenuation of prolonged oxidative stress are favorable for inflammation resolution and M2-associated tissue repair [34, 35]. In this context, we propose that the

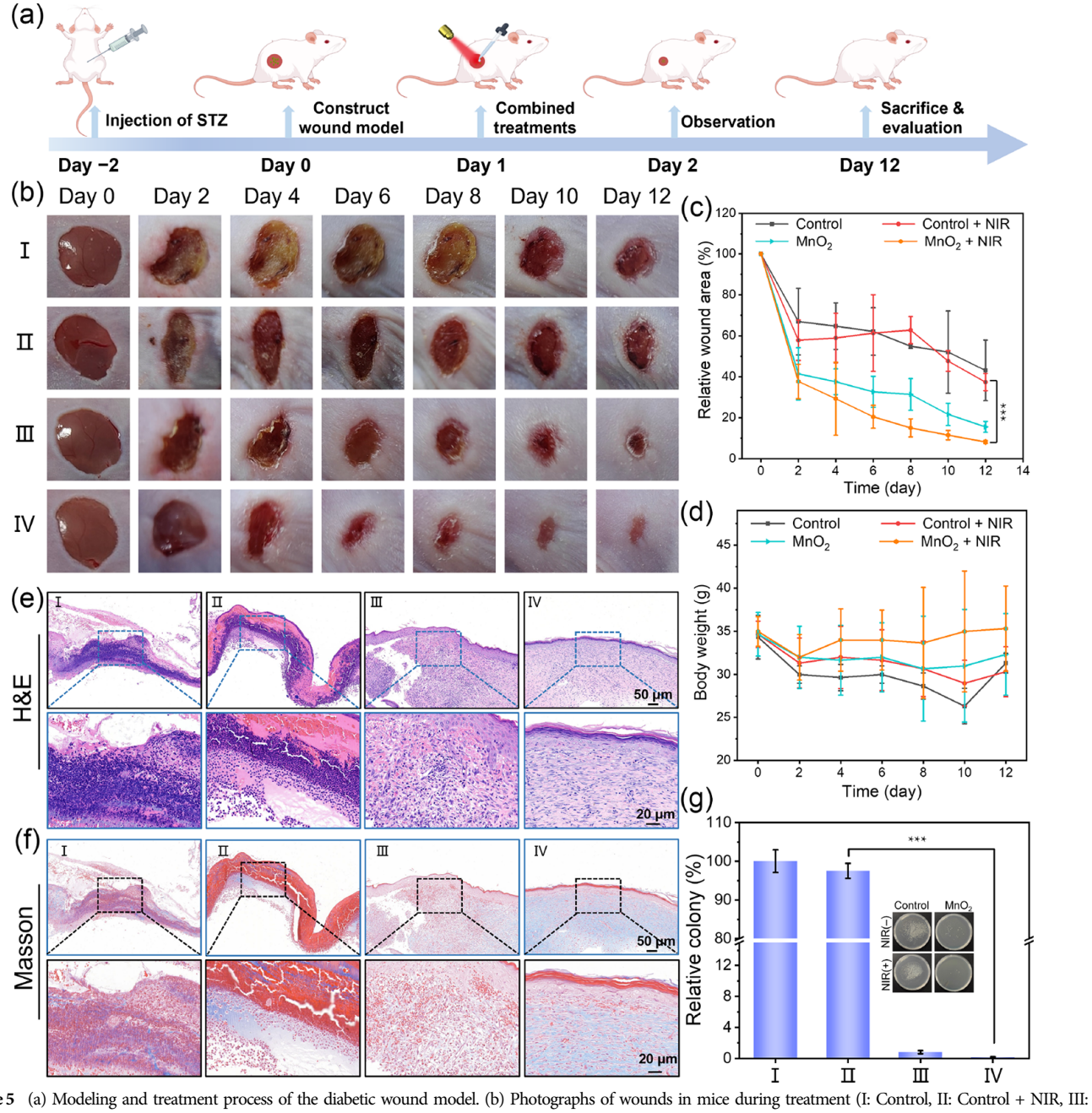

Figure 5 (a) Modeling and treatment process of the diabetic wound model. (b) Photographs of wounds in mice during treatment (I: Control, II: Control + NIR, III: MnO_2 aerogels, VI: MnO_2 aerogels + NIR). Differences in the relative (c) wound dimensions and (d) body weight of mice subjected to different treatments. (e) H&E staining and (f) Masson's trichrome staining of mouse wound sections on day 12. (g) Photographs and bacterial quantification of mouse wound-coated plates at the end of treatment. $^{*}P < 0.05$, $^{**}P < 0.01$, $^{***}P < 0.001$.

MnO_2 aerogels may regulate macrophage behavior through a two-stage effect: on the one hand, their OD-like antibacterial activity helps control wound infection in the early stage; on the other hand, their CAT-, SOD-, and GPX-like activities help decompose excessive ROS and alleviate oxidative stress in the wound microenvironment, thereby creating conditions that are more favorable for the transition toward a reparative M2-like phenotype. Therefore, we examined the expression levels of the macrophage phenotypic markers CD86 (M1) and CD206 (M2). The results showed that the CD206/CD86 ratio in the MnO_2 aerogels + NIR group was significantly increased compared with the Control group (Fig. S17 in the ESM), indicating that MnO_2 aerogels modulate the direction of macrophage polarization, shifting the immune response from a pro-inflammatory state toward a reparative state, thereby alleviating inflammation while promoting tissue regeneration and accelerating wound healing. The effective alleviation of inflammation created a favorable microenvironment for subsequent tissue repair. We further examined the expression level of the inflammatory factor TNF-α. The MnO_2 aerogels + NIR group exhibited significantly reduced TNF-α expression, consistent with minimal inflammatory cells observed in H&E-stained tissue sections, indicating superior antibacterial effects and inflammation attenuation (Fig. 6(a)). Angiogenesis, critical for diabetic wound repair, was assessed via VEGF, α-SMA, and CD31 staining. The

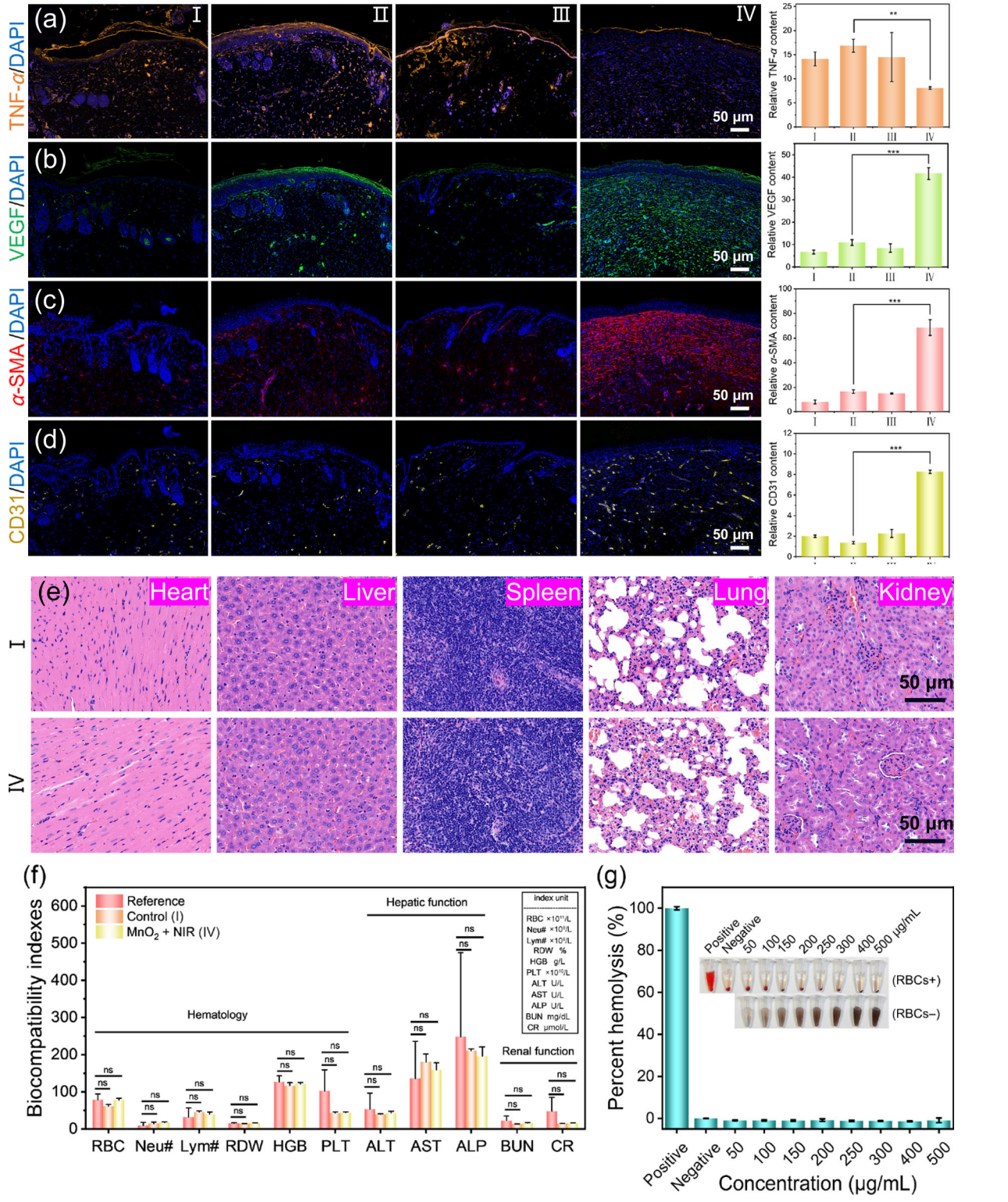

Figure 6 Immunofluorescence staining and quantitative analysis of (a) TNF-α, (b) VEGF, (c) α-SMA, and (d) CD31 at the wound site in various groups (I: Control, II: Control + NIR, III: MnO_2 aerogels, VI: MnO_2 aerogels + NIR) at the end of treatment, $^*P < 0.05$, $^{**}P < 0.01$, $^{***}P < 0.001$. (e) H&E-stained sections of vital organs of mice in control and MnO_2 aerogels + NIR groups. (f) Analysis of routine blood and biochemical indicators. (g) Hemolysis test of MnO_2 aerogels.

MnO_2 aerogels + NIR group showed the highest VEGF expression, reflecting enhanced blood vessel formation, and elevated α-SMA and CD31 levels, confirming robust revascularization compared to moderate expression in the MnO_2 aerogels group and low expression in the control group (Figs. 6(b)–6(d)). This revascularization likely results from the CAT-like activity of MnO_2 aerogels, which decomposes H_2O_2 to produce O_2, alleviating hypoxia in the infected microenvironment.

Biosafety was evaluated via H&E staining of major organs (heart, liver, spleen, lungs, kidneys) from the Control and MnO_2 aerogels +

NIR groups, showing no pathological damage or inflammation (Fig. 6(e)). Blood physiological parameters were within normal ranges, with no significant differences between the two groups (Fig. 6(f)). A hemolysis assay confirmed that MnO_2 aerogels (500 μg/mL) did not induce detectable red blood cell hemolysis (Fig. 6(g)). Next, live/dead cell staining experiments were conducted using normal mouse hepatocytes (AML-10 cells). The results showed that at MnO_2 aerogels concentrations greater than 200 μg/mL, most cells exhibited green fluorescence (live cells), while red fluorescence (dead cells) was nearly undetectable (Fig. S18 in the ESM). These results indicate that MnO_2 aerogels are a low-toxicity nanozyme candidate for the infection treatment and healing of diabetic wounds.

3 Conclusions

In this study, we developed a multifunctional MnO_2 aerogel as an integrated platform for regulating the complex microenvironment of chronic diabetic wounds. Benefiting from its three-dimensional interconnected network, hierarchical porosity, and nanoflower-like morphology, the MnO_2 aerogel provides efficient exposure of catalytic sites and diffusion of reactants, thereby enabling precise modulation of reactive oxygen species and glucose levels at the wound site. The MnO_2 aerogel exhibits five enzyme-mimicking activities—oxidase, glucose oxidase, glutathione peroxidase, catalase, and superoxide dismutase—allowing dynamic and stage-specific regulation of ROS. In the early stage, its oxidase- and GOx-like activities promote antibacterial effects by generating $\cdot O_2^-$ and consuming excess glucose, while GPX-like activity depletes glutathione to further amplify oxidative stress against pathogens. Upon NIR irradiation, the aerogel's strong photothermal responsiveness disrupts bacterial membranes, enhances biofilm eradication, and synergistically strengthens ROS-mediated sterilization without the need for exogenous H_2O_2. At later stages, the CAT- and SOD-like activities of the MnO_2 aerogel scavenge excessive ROS and produce O_2, alleviating hypoxia, restoring redox homeostasis, and creating a favorable environment for tissue repair. *In vivo*, these coordinated functions translate into significantly reduced inflammation, re-established glucose and redox balance, and enhanced angiogenesis and tissue regeneration, as evidenced by the downregulation of TNF-α and upregulation of VEGF, α-SMA, and CD31. Consequently, MnO_2 aerogel treatment, especially in combination with NIR irradiation, markedly accelerates wound closure in diabetic models. Overall, this work demonstrates that MnO_2-based metallic oxide aerogels represent a promising and versatile platform for advanced diabetic wound therapy. By integrating antibacterial, glucose-regulating, antioxidant, and pro-regenerative functions within a single material, this strategy offers a comprehensive approach to overcoming the multifactorial barriers that hinder diabetic wound healing and may be extended to the treatment of other chronic inflammation-associated conditions.

4 Experimental

4.1 Chemicals

Manganese (II) chloride ($MnCl_2$), 3,3',5,5'-tetramethylbenzidine (TMB), and DMF were acquired from Adamas-Beta Co., Ltd. (Shanghai, China). Potassium permanganate ($KMnO_4$) was purchased from General Reagent Co., Ltd. (Shanghai, China). DTNB was procured from Aladdin Co., Ltd. (Shanghai, China). Reduced GSH was purchased from Sigma-Aldrich Co., Ltd. (Shanghai, China). STZ was obtained from Macklin Co., Ltd. (Shanghai, China). A live/dead bacteria staining kit was obtained from BestBio Scientific Co., Ltd. (Shanghai, China). The SOD activity assay kit was obtained from Solarbio Co., Ltd. (Beijing, China). MRSA, ATCC 43300 and *Pseudomonas aeruginosa* (ATCC 9027) were acquired from the American Type Culture Collection (ATCC). All chemicals were used without further purification.

4.2 Instruments

Transmission electron microscopy (TEM), high-resolution transmission electron microscopy (HRTEM), and selected-area electron diffraction (SAED) were carried out with a JEM 2100F (JEOL, Japan). Scanning electron microscopy (SEM) was conducted using an EV010 machine (Zeiss, Germany). X-ray photoelectron spectroscopy (XPS) measurements were performed on a Thermo Scientific K-Alpha with the C 1s peak at 284.8 eV used as the binding energy reference. UV–Vis absorption spectra were acquired using a MAPADA UV-3200S spectrometer (Shanghai, China). Dissolved oxygen was measured using a portable dissolved oxygen meter (Lei-ci JPBJ-608, Shanghai, China). A Fotric 225s infrared thermal imaging camera (MDL-XF-808, Changchun, China) was used to monitor the temperature changes under near-infrared (NIR) laser irradiation. Fluorescence images were acquired using a laser confocal scanning microscope (Zeiss LSM980, Germany). Bacterial morphology was analyzed using a scanning electron microscope (SU8100, Japan). Blood glucose levels in mice were monitored using a commercial glucometer (Sinocare, China).

4.3 Synthesis of MnO_2 aerogels

Briefly, 0.114 g $MnCl_2$ (18.1 mM) was quickly dissolved in 50 mL of dimethylformamide (DMF) and stirred vigorously at 50 °C for 1 min. $KMnO_4$ solution (5 mL, 20 mg/mL) was then rapidly injected, and the reaction continued for 30 min, forming MnO_2 ultrathin nanosheets that self-assembled into nanoflowers in the resulting water/DMF mixture via freeze-thaw technique. The obtained product was centrifuged, washed three times with deionized water, dispersed in ultrapure water, frozen in liquid nitrogen, and lyophilized in a freeze-dryer to obtain MnO_2 aerogels.

4.4 Evaluation of multienzyme-like activity of MnO_2 aerogels

The OD-like activity was assessed by mixing 50 μL of TMB (10 mM), 50 μL of MnO_2 aerogels (100 μg/mL), and 900 μL of HAc-NaAc buffer (0.2 M, pH 5.0). After a 3-min reaction, the reaction mixture absorbance was measured using UV–Vis spectrophotometry. The CAT-like activity was evaluated by monitoring H_2O_2 absorbance at 240 nm. Three groups were prepared: (i) H_2O_2 (0.1 M, 50 μL), (ii) MnO_2 aerogels (100 μg/mL, 50 μL), and (iii) H_2O_2 + MnO_2 aerogels, in 950 μL of HAc-NaAc buffer (0.2 M, pH 5.0). Absorbance was recorded using UV–Vis spectrophotometry. Additionally, the O_2 generated during the reaction was quantified using a portable dissolved oxygen meter. MnO_2 aerogels (10 mg/mL, 100 μL) were added to 50 mL of H_2O_2 solutions (0–100 mM), and dissolved oxygen changes were monitored for 3 min. The SOD-like activity was determined using a commercial SOD assay kit (Solarbio, Beijing). The assay quantifies O_2^- scavenging by monitoring the reduction of nitroblue tetrazolium to formazan, which absorbs at 560 nm. MnO_2 aerogels at varying concentrations were tested, with decreased absorbance indicating O_2^- scavenging activity. The GOx-like activity was

verified through pH changes in a glucose solution (1 mL, 0.1 M, O_2-saturated) incubated with MnO_2 aerogels (20–1000 μg/mL, 1 mL) at 37 °C for 30 min. Following incubation, the supernatant was spun in a centrifuge, and pH was measured. GPX-like activity was evaluated by monitoring GSH consumption using DTNB as a chromogenic probe. MnO_2 aerogels (50, 100, 200, 500 μg/mL, 100 μL) were incubated with 1 mM GSH for varying durations. Then, PBS (900 μL) and DTNB (10 μL, 0.1 mM) were added. After 3 min, absorption spectra (300–550 nm) were generated using UV–Vis spectrophotometry.

Aqueous dispersions of MnO_2 aerogels (1 mL; 0, 10, 20, 50, 100, 200, 250 μg/mL) were exposed to irradiation from 808 nm laser (1.0 W/cm^2) for 10 min. The effect of varying laser power densities (0.5, 0.75, 1.0, 1.5 W/cm^2) was tested at 200 μg/mL. Temperature elevation was monitored in real time using an infrared thermal camera. Photothermal conversion efficiency (η) was calculated using Eq. (1):

$$\eta = \frac{h \cdot s(T_{max} - T_{surr}) - Q_0}{I(1 - 10^{-A})} \quad (1)$$

In this equation, where h represents the heat transfer coefficient, s denotes the sample surface area, T_{max} is the peak temperature, T_{surr} is the ambient temperature, Q_0 is the background heat dissipation, I stands for the laser power density, and A is the absorbance at 808 nm.

4.5 *In vitro* antibacterial effect of MnO_2 aerogels

4.5.1 Bacterial plate counting

Overnight incubation of methicillin-resistant *Staphylococcus aureus* (MRSA, Gram-positive) and *Pseudomonas aeruginosa* (*P. aeruginosa*, Gram-negative) suspensions was carried out at 37 °C and 120 rpm using a constant-temperature shaker. Each bacterial suspension (1 × 10^7 CFU/mL) was divided into eight treatment groups: (I) Control, (II) Control + NIR, (III) Oxygenated PBS (OP), (IV) OP + NIR, (V) MnO_2 aerogels, (VI) MnO_2 aerogels + NIR, (VII) MnO_2 aerogels (OP), and (VIII) MnO_2 aerogels (OP) + NIR. MnO_2 aerogels were used at a final concentration of 200 μg/mL. After 1 h of incubation at 37 °C, the bacterial suspensions were treated with or without 808 nm laser irradiation (1.0 W/cm^2) for 10 min. The suspensions were then diluted, spread on agar plates, and incubated at 37 °C for 18 h. Colony counts were used to calculate bacterial viability: Viability (%) = (C_t/C_0) × 100 (mean ± SD, n = 3), where C_0 and C_t represent colony counts in the control and experimental groups, respectively.

4.5.2 Live/dead staining

Bacterial membrane integrity was assessed using a Live/Dead viability kit with N01 and propidium iodide (PI) to label live (green fluorescence) and dead (red fluorescence) bacteria, respectively. MRSA and *P. aeruginosa* suspensions (1 × 10^8 CFU/mL) underwent the same eight treatments as above. After treatments, samples were stained with 1.5 μL of N01 and 2 μL of PI for 30 min in the dark and visualized using laser confocal scanning microscopy.

4.5.3 Bacterial morphology

Morphological changes were examined via SEM. After treatments, bacterial suspensions were centrifuged (3000 rpm, 5 min), and the supernatant was discarded. Pellets were treated with 500 μL of 2.5% glutaraldehyde at 4 °C for 4 h, followed by sequential dehydration in 10%, 30%, 50%, 70%, 90%, and 100% ethanol (10 min each). Samples were then analyzed by SEM.

4.5.4 ROS staining test

ROS production was evaluated using 20 μM DCFH-DA. After treatments, samples were incubated with DCFH-DA for 20 min in the dark, washed with PBS to remove unbound dye, and analyzed for fluorescence intensity via laser confocal scanning microscopy.

4.6 Biofilm inhibition

4.6.1 Crystal violet staining

MRSA and *P. aeruginosa* biofilms were cultured in 96-well plates for 48 h at 37 °C. Biofilms were subjected to different treatments for 4 h as described above. The remaining biofilms were fixed with 4% paraformaldehyde for 30 min, stained with crystal violet for 15 min, and washed with PBS. Biofilms that were stained were decolorized using 95% ethanol, and absorbance was read at 590 nm with a microplate reader.

4.6.2 Live/dead staining of biofilms

For 48 h, biofilms of MRSA and *P. aeruginosa* were cultured in glass-bottom cell culture dishes. After applying the same eight treatments as above, biofilms were treated with 5 μL of N01 and 5 μL of PI for 30 min in the dark. Following PBS washing, biofilms were visualized using laser confocal scanning microscopy to assess live (green) and dead (red) bacteria, as well as biofilm thickness changes.

4.7 *In vivo* MRSA-infected animal wound healing

All animal procedures received approval from the Institutional Animal Care and Use Committee of the University of South China and were performed in line with its guidelines. A diabetic mouse model was established by intraperitoneally injecting STZ (120 mg/kg in 0.1 M sodium citrate buffer, pH 4.5) into male Kunming mice (8–10 weeks old). After 48 h, blood glucose levels were measured via tail vein sampling using a glucose meter, with levels ≥ 16.7 mM confirming diabetes. Following depilation, an 8 mm wound was formed on the back of anesthetized mice and inoculated with 50 μL of MRSA suspension (1 × 10^8 CFU/mL). After 24 h, mice were randomly allocated to four groups (n = 3): (I) Control, (II) Control + NIR, (III) MnO_2 aerogels, and (IV) MnO_2 aerogels + NIR. For groups III and IV, 100 μL of MnO_2 aerogels (200 μg/mL) was applied to the wound. Groups II and IV received 808 nm laser irradiation (1.0 W/cm^2) for 10 min, with wound temperature monitored in real time using an infrared thermal camera. Wound areas and body weights were recorded every other day, and digital photographs of the wounds were taken. On day 12, mice were euthanized, and wound tissues were harvested for histological analysis (H&E and Masson's trichrome staining) and immunofluorescence staining (α-SMA, CD31, TNF-α, VEGF). Major organs (heart, liver, spleen, lungs, kidneys) were collected for histopathological evaluation to assess the systemic biosafety of MnO_2 aerogels.

4.8 Statistical analysis

The results are expressed as mean ± standard deviation (SD) and were processed with Origin software. Student's t-test was used for comparing two groups, whereas one-way ANOVA with an LSD post hoc test was applied for assessing differences among three or

more groups. Significance was denoted by ns (non-significance), *P < 0.05, **P < 0.01, ***P < 0.001. P < 0.05 was considered statistically significant.

Electronic Supplementary Material: Supplementary material (further details of SAED measurements, N_2 adsorptiondesorption isotherms, pore distributions, ESR detection, photothermal thermal measurements, Lineweaver Burk curves, biofilm eradication, immunofluorescence images, and Live/Dead cell staining) is available in the online version of this article at https://doi.org/10.26599/NR.2026.94908653.

Data availability

The data are available from the corresponding author on reasonable request.

Acknowledgements

The authors acknowledge financial support from the High-Level Talent Development Scheme of the Hunan Provincial Hospital of Maternal and Child Health Care, the National Natural Science Foundation of China (No. 22374065), the Outstanding Youth Foundation of Hunan Province (No. 2024JJ2047), the Natural Science Foundation of Hunan Province of China (No. 2025JJ50563), the Aid Program for Science and Technology Innovative Research Teams in Higher Educational Institutions of Hunan Province, FuRong Young Scholar Program of Hunan Province (No. 2025QT-66), Scientific Research Fund of Hunan Province Education Department (No. 25A0341), and Interdisciplinary Research Program in Medicine and Engineering, The First Affiliated Hospital of University of South China (No. IRP-M&E-2025-08). The authors extend their gratitude to Shiyanjia Lab (from Scientific Compass www.shiyanjia.com) for providing invaluable assistance with the XPS, SEM, and TEM tests.

Declaration of competing interest

All the contributing authors report no conflict of interests in this work.

Author contribution statement

Q. L. Y., X. F. T., and M. H. W. conceived and designed the experiments. M. H. W., J. K. Z., D. J. R., Y. X. C., S. H. S., W. X. Q., H. Y. G., and W. C. W. performed the experiments. M. H. W. and X. F. T. analyzed the data. M. H. W., J. T., X. F. T., and Q. L. Y. wrote the manuscript. All authors were involved in discussing the results and commenting on the manuscript throughout its preparation.

Informed consent

Not applicable.

Ethics statement

The animal experiments were carried out following the guidelines of the University of South China Institutional Committee for the Care and Use of Laboratory Animals and were approved by the Committee on Ethical Use of Animals of University of South China (Ethical code: 2023027).

Use of AI statement

None.

References

[1] Xu, Y.; Lu, J. L.; Li, M.; Wang, T. G.; Wang, K.; Cao, Q. Y.; Ding, Y.; Xiang, Y.; Wang, S. Y.; Yang, Q. Q. et al. Diabetes in China part 2: Prevention, challenges, and progress. *Lancet Public Health* **2024**, *9*, e1098–e1104.

[2] Xu, Y.; Lu, J. L.; Li, M.; Wang, T. G.; Wang, K.; Cao, Q. Y.; Ding, Y.; Xiang, Y.; Wang, S. Y.; Yang, Q. Q. et al. Diabetes in China part 1: Epidemiology and risk factors. *Lancet Public Health* **2024**, *9*, e1089–e1097.

[3] Yu, M. G.; Gordin, D.; Fu, J. L.; Park, K.; Li, Q.; King, G. L. Protective factors and the pathogenesis of complications in diabetes. *Endocr. Rev.* **2024**, *45*, 227–252.

[4] Huang, F.; Lu, X. Y.; Yang, Y.; Yang, Y. S.; Li, Y. Y.; Kuai, L.; Li, B.; Dong, H. Q.; Shi, J. L. Microenvironment‐based diabetic foot ulcer nanomedicine. *Adv. Sci.* **2023**, *10*, 2203308.

[5] Shi, Q. Y.; Nong, K. L.; Vandvik, P. O.; Guyatt, G. H.; Schnell, O.; Rydén, L.; Marx, N.; Brosius, F. C.; Mustafa, R. A.; Agarwal, A. et al. Benefits and harms of drug treatment for type 2 diabetes: Systematic review and network meta-analysis of randomised controlled trials. *BMJ* **2023**, *381*, e074068.

[6] ElSayed, N. A.; Aleppo, G.; Aroda, V. R.; Bannuru, R. R.; Brown, F. M.; Bruemmer, D.; Collins, B. S.; Cusi, K.; Das, S. R.; Gibbons, C. H. et al. Summary of revisions: *Standards of care in diabetes*—2023. *Diabetes Care* **2023**, *46*, S5–S9.

[7] Bi, S. W.; He, C. Y.; Zhou, Y. N.; Liu, R. Q.; Chen, C.; Zhao, X. S.; Zhang, L.; Cen, Y.; Gu, J.; Yan, B. Versatile conductive hydrogel orchestrating neuro-immune microenvironment for rapid diabetic wound healing through peripheral nerve regeneration. *Biomaterials* **2025**, *314*, 122841.

[8] Kang, Y.; Xu, L. L.; Dong, J. R.; Yuan, X.; Ye, J. M.; Fan, Y. Y.; Liu, B.; Xie, J. L.; Ji, X. Y. Programmed microalgae-gel promotes chronic wound healing in diabetes. *Nat. Commun.* **2024**, *15*, 1042.

[9] Wei, Q. L.; Zhu, J. Q.; Liu, M.; E, Y. X.; Deng, Q. Y.; Meng, X. B.; Liu, C. Z.; Li, M. T. Turning gold nanoflowers from prooxidant to plasmon-enhanced antioxidant for diabetic wound therapy. *Nano Res.* **2026**, *19*, 94908313.

[10] Tan, X. F.; Lin, N. Y.; Yang, S.; Gong, H. Y.; Wang, M. H.; Li, N.; Liu, F.; Rao, D. J.; Wu, Y. Y.; Tang, J. et al. AuCu@CuO_2 aerogels with H_2O_2/O_2 self-supplying and quadruple enzyme-like activity for *MRSA*-infected diabetic wound management. *Adv. Sci.* **2025**, *12*, 2502391.

[11] Li, H.; Wei, S. Z.; Ling, Q. J.; Wang, R. N.; Liu, T. Z.; Yu, H.; Zhao, P. C.; Zhang, K. Y.; Bian, L. M.; Liao, W. M. Nanozyme-reinforced hydrogel spray as a reactive oxygen species-driven oxygenator to accelerate diabetic wound healing. *Adv. Mater.* **2025**, *37*, 2504829.

[12] Liang, X. Y.; Chen, H. G.; Zhang, R.; Xu, Z. X.; Zhang, G.; Xu, C.; Li, Y.; Zhang, L.; Xu, F. J. Herbal micelles-loaded ROS-responsive hydrogel with immunomodulation and microenvironment reconstruction for diabetic wound healing. *Biomaterials* **2025**, *317*, 123076.

[13] Yang, H.; Lv, D. M.; Qu, S. Q.; Xu, H. L.; Li, S. T.; Wang, Z. Y.; Cao, X. L.; Rong, Y. C.; Li, X. H.; Wu, H. L. et al. A ROS-responsive lipid nanoparticles release multifunctional hydrogel based on microenvironment regulation promotes infected diabetic wound healing. *Adv. Sci.* **2024**, *11*, 2403219.

[14] Liu, J. T.; Han, X. Y.; Zhang, T. Y.; Tian, K. Y.; Li, Z. P.; Luo, F. Reactive oxygen species (ROS) scavenging biomaterials for anti-inflammatory diseases: From mechanism to therapy. *J. Hematol. Oncol.* **2023**, *16*, 116.

[15] D'agostino, M.; Sileno, S.; Lulli, D.; De Luca, N.; Scarponi, C.; Teson, M.; Torcinaro, A.; De Santa, F.; Cirielli, C.; Furgiuele, S. et al. miR-200c inhibition and catalase accelerate diabetic wound healing. *J. Biomed. Sci.* **2025**, *32*, 21.

[16] Shen, Z. H.; Du, L.; Fang, X. W.; Zhang, Z.; Li, X. K.; Xiao, S. C.; Xiao, J.; Chen, S. X. Nanozyme cryogel accelerates diabetic wound healing by targeting biofilms and inflammations of the wound bed. *ACS Nano* **2025**, *19*, 35081–35101.

[17] Yang, H.; Chen, Y. F.; Rong, Y. C.; Zhou, Y. X.; Li, S. T.; Li, X. H.; Wu, H. L.; Lv, D. M.; Cao, X. L.; Wang, P. et al. Multifunctional hydrogel targeting senescence to accelerate diabetic wound healing through promoting angiogenesis. *J. Nanobiotechnol.* **2025**, *23*, 177.

[18] He, J. H.; Du, M. X.; Makvandi, P.; Xu, Y.; He, X. J.; Jin, X. R. NIR-II-enhanced Pt–MoS_2 nanozymes for synergistic photothermal and chemodynamic therapy against methicillin-resistant *Staphylococcus aureus* to promote wound healing. *Nano Res.* **2025**, *18*, 94907538.

[19] Capó, X.; Monserrat-Mesquida, M.; Quetglas-Llabrés, M.; Batle, J. M.; Tur, J. A.; Pons, A.; Sureda, A.; Tejada, S. Hyperbaric oxygen therapy reduces oxidative stress and inflammation, and increases growth factors favouring the healing process of diabetic wounds. *Int. J. Mol. Sci.* **2023**, *24*, 7040.

[20] Chen, J.; Qu, B. Q.; Yang, D. Y.; Wang, Y. Z.; Zhu, H. Y.; Wang, Z. C.; Zhang, X. W.; Ma, H. K.; Zhao, N.; Zhao, L. et al. Combined metabolomics and network pharmacology to elucidate the mechanisms of Huiyang Shengji decoction in treating diabetic skin ulcer mice. *Phytomedicine* **2025**, *141*, 156569.

[21] Liu, C. J.; Liu, K.; Zhang, D.; Liu, Y. T.; Yu, Y. F.; Kang, H. F.; Dong, X. Z.; Dai, H. L.; Yu, A. X. Dual-layer microneedles with NO/O_2 releasing for diabetic wound healing via neurogenesis, angiogenesis, and immune modulation. *Bioact. Mater.* **2025**, *46*, 213–228.

[22] Qi, X. L.; Cai, E. Y.; Xiang, Y. J.; Zhang, C. F.; Ge, X. X.; Wang, J. J.; Lan, Y. L.; Xu, H. B.; Hu, R. D.; Shen, J. L. An immunomodulatory hydrogel by hyperthermia-assisted self-cascade glucose depletion and ROS scavenging for diabetic foot ulcer wound therapeutics. *Adv. Mater.* **2023**, *35*, 2306632.

[23] Wang, Q.; Luo, Z.; Li, Z. G.; Hu, H. H.; Lin, Y. T.; Fan, X. T.; Li, Z. B.; Wu, Y. L. *In-situ* oxygen-supplying ROS nanopurifier for enhanced healing of MRSA-infected diabetic wounds via microenvironment modulation. *Acta Biomater.* **2025**, *193*, 334–347.

[24] Xiong, Y.; Chu, X. Y.; Yu, T.; Knoedler, S.; Schroeter, A.; Lu, L.; Zha, K.; Lin, Z.; Jiang, D. S.; Rinkevich, Y. et al. Reactive oxygen species-scavenging nanosystems in the treatment of diabetic wounds. *Adv. Healthcare Mater.* **2023**, *12*, 2300779.

[25] Zhou, Q. L.; Zhuang, Y.; Deng, X. L.; Jiang, W. D.; Wang, X. D.; Yuan, C. Y.; Lin, K. L. Hydrogel-based ROS-regulating strategy: Reprogramming the oxidative stress imbalance in advanced diabetic wound repair. *Adv. Mater.* **2026**, *38*, e12719.

[26] Tang, Y. J.; Liu, X. P.; Qi, P. C.; Cai, Y. J.; Wang, H. J.; Qin, Y.; Gu, W. L.; Wang, C. L.; Sun, Y.; Zhu, C. Z. Single-atom Ce-doped metal hydrides with high phosphatase-like activity amplify oxidative stress-induced tumor apoptosis. *ACS Nano* **2024**, *18*, 25685–25694.

[27] Yang, L. X.; Jing, F. Y.; Liu, T.; Zhao, X. C.; Chen, A. B.; Zhang, T. Z. Antioxidant nanozyme-protected mesenchymal stem cells loaded on photo-crosslinked microsphere blocks for inflammatory deep tissue repair. *Nano Res.* **2026**, *19*, 94908119.

[28] Li, Q. L.; Dong, M. D.; Han, Q. Q.; Zhang, Y. J.; Yang, D. Z.; Wei, D. Q.; Yang, Y. L. Enhancing diabetic wound healing with a pH-responsive nanozyme hydrogel featuring multi-enzyme-like activities and oxygen self-supply. *J. Controlled Release* **2024**, *365*, 905–918.

[29] Li, Z. Y.; Ding, B. B.; Li, J.; Chen, H.; Zhang, J. S.; Tan, J.; Ma, X. Y.; Han, D.; Ma, P. A.; Lin, J. Multi-enzyme mimetic MoCu dual-atom nanozyme triggering oxidative stress cascade amplification for high-efficiency synergistic cancer therapy. *Angew. Chem., Int. Ed.* **2025**, *64*, e202413661.

[30] Long, M. M.; Wang, L. T.; Kang, L. N.; Liu, D. F.; Long, T. T.; Ding, H.; Duan, Y. F.; He, H. L.; Xu, B.; Gu, N. Prussian blue nanozyme featuring enhanced superoxide dismutase-like activity for myocardial ischemia reperfusion injury treatment. *ACS Nano* **2025**, *19*, 4561–4581.

[31] Cheng, Z. Y.; Lu, J. L.; Ran, W.; Rong, S. P. Cation-induced self-assembly of α-MnO_2 nanowires into high-purity self-standing three-dimensional network aerogels for catalytic decomposition of carcinogenic formaldehyde at ambient temperature. *ACS Appl. Mater. Interfaces* **2024**, *16*, 46247–46258.

[32] Chen, Y. D.; Liu, Q. X.; Guan, J. J.; Zheng, C. Y.; Shi, S. M.; Zheng, W. W.; Guan, J. Z.; Mao, Y. J. Rescuing inflammatory microenvironment induced senescence via MgO immune mediated asymmetric short fibers for accelerating diabetic wound repair. *Mater. Today Bio* **2025**, *33*, 102079.

[33] Sheng, J. Y.; Wu, Y. H.; Ding, H.; Feng, K. Z.; Shen, Y.; Zhang, Y.; Gu, N. Multienzyme-like nanozymes: Regulation, rational design, and application. *Adv. Mater.* **2024**, *36*, 2211210.

[34] Li, X. Y.; Gao, J. J.; Wu, C. C.; Wang, C. Y.; Zhang, R. S.; He, J.; Xia, Z. J.; Joshi, N.; Karp, J. M.; Kuai, R. Precise modulation and use of reactive oxygen species for immunotherapy. *Sci. Adv.* **2024**, *10*, eadl0479.

[35] Li, C. L.; Deng, C. S.; Wang, S. W.; Dong, X.; Dai, B.; Guo, W. D.; Guo, Q. Q.; Feng, Y. L.; Xu, H. D.; Song, X. Y. et al. A novel role for the ROS-ATM-Chk2 axis mediated metabolic and cell cycle reprogramming in the M1 macrophage polarization. *Redox Biol.* **2024**, *70*, 103059.